Electronic Supplementary Material (ESI) for Sustainable Energy & Fuels.
This journal is © The Royal Society of Chemistry 2022

Electronic Supplementary Information

Hydrated Lithium *nido*-Boranes for Solid-Liquid Hybrid Batteries

Diego H. P. Souza,[a] Terry D. Humphries,[a] Yu Liu,[a] Anton Gradišek,[b] Anita M. D'Angelo,[c] Craig E. Buckley,[a] and Mark Paskevicius[a]*

[a.] Department of Physics and Astronomy, Curtin University, GPO Box U1987, Perth, WA 6845, Australia.

[b.] Jožef Stefan Institute, SI-1000 Ljubljana, Slovenia.

[c.] Australian Synchrotron (ANSTO), Clayton, VIC 3168, Australia.

* Corresponding author. *E-mail address:* m.paskevicius@curtin.edu.au.

EXPERIMENTAL SECTION

Raman Spectroscopy

Raman spectra were obtained with an Alpa300SAR+ confocal Raman microscope (WITEC GmbH, Ulm, Germany) equipped with a 2w-NdYAG laser (532 nm wavelength) and a 20x/0.4 NA objective (Zeiss, Germany). The spectrometer utilises a 600 g mm^{-1} grating. Powder samples were packed in capillaries inside an argon filled glovebox (Mbraun, O_2 & H_2O < 1 ppm), sealed with grease and then flame-sealed. Spectra were recorded with 100 accumulations at an integration time of 400 ms. Data were processed in terms of background subtraction, cosmic ray removal and exported with the ProjectFOUR software package (WITec, Ulm, Germany).

Nuclear Magnetic Resonance (NMR) Spectroscopy

A Bruker Avance III 400 MHz NanoBay spectrometer was used to collect $^{11}B\{^1H\}$ (128 MHz) NMR data at room temperature (RT). The powdered samples were dissolved in 600 µL of deuterated solvent (D_2O or CD_3CN) prior to analysis. In case of a solution-state sample, an aliquot of 100 µL was dissolved in 600 µL of its deuterated solvent and analysed. The ^{11}B NMR spectra were referenced to a boron trifluoride etherate ($BF_3O(C_2H_5)_2$) external standard.

^{11}B (128.29 MHz) solid-state NMR spectroscopy was performed on a Varian VNMRS spectrometer at RT. The samples were packed inside a 4 mm zirconia rotor in an argon filled glovebox and sealed with gas-tight inserts. The samples were spun at 5 kHz, and acquisition

was performed with a one-pulse sequence, with proton decoupling and a relaxation delay of 10 seconds, for a total of 50 transients.

^{11}B spin-lattice NMR relaxation rates (T_1^{-1}) of *b*-$LiB_{11}H_{14}\cdot(H_2O)_n$ were measured as a function of temperature in a heating run from -190 to 110 °C (setup limit) using a 4.7 T superconducting magnet, corresponding to the ^{11}B Larmor frequency of 64.168 MHz. This approach has been previously successfully attempted on similar systems, such as $(NH_4)_2B_{12}H_{12}$,[1,2] $(NH_4)_2B_{10}H_{10}$,[2] and $Ag_2B_{12}H_{12}$.[3] Spin-lattice relaxation rates were measured using a saturation-recovery sequence with spin echoes to detect the signal. The relaxation recovery data is well-described using a stretch-exponent function.

Structural Characterisation

X-Ray Powder Diffraction (XRPD) measurements were performed at room temperature (RT) on a Bruker D8 Advance Powder Diffractometer with a Cu K_α radiation source (λ = 1.54056 Å) operated at 40 kV/40mA with a LynxEye detector in the 2ϑ range of 5 − 60°. The powder was mounted inside an argon glovebox on a single-crystal Si low background sample holder and sealed with an airtight poly(methyl-methacrylate) (PMMA) dome. Broad diffraction halos from the sample holder are seen at ~10° and ~20° 2ϑ in the diffraction data.

The samples *a*-$LiB_{11}H_{14}\cdot(H_2O)_n$ and *b*-$LiB_{11}H_{14}\cdot(H_2O)_n$ were also characterised using Synchrotron Radiation X-ray Powder Diffraction (SR-XRPD) that was collected at the powder diffraction beamline at the Australian Synchrotron using a wavelength of λ = 0.590827(4) Å, which was refined using a NIST LaB_6 660b line position standard. The samples were ground in a mortar and pestle and mounted into a 1.0 mm borosilicate capillary inside an argon glovebox, sealed with grease and flame-sealed outside the glovebox. Data was collected on a Mythen II microstrip detector at two positions, and later combined into gap-free data sets, from 1° – 81° 2ϑ. *In-situ* SR-XRPD data for *a*-$LiB_{11}H_{14}\cdot(H_2O)_n$ were collected during heating and cooling, where the sample was heated from 25 °C to 100 °C at 5 °C min^{-1} and then cooled at 6 °C min^{-1} to RT. *In-situ* SR-XRPD data for *b*-$LiB_{11}H_{14}\cdot(H_2O)_n$ was collected during cooling to -175 °C at 1 °C min^{-1}. Temperature was controlled using an Oxford Cryosystems Cryostream Plus.

Diffraction patterns were indexed and quantitative analysis performed with the Rietveld method using Bruker Topas software. The refinement of the samples was conducted without the use of an internal/external standard. The percentage of each phase is based on the crystalline components only and does not take into account unidentified phases or amorphous material.[4] Reported uncertainties are based on mathematical fitting uncertainty in Topas software.

Simultaneous Differential Scanning Calorimetry (DSC) and Thermogravimetry Analysis (TGA)

Measurements were performed with a Netzsch (STA 449 F3 Jupiter) under an argon flow of 40 mL min^{-1} using Al_2O_3 crucibles containing approximately 7 mg of sample in a Pt furnace. The analysis was conducted from 25 – 300 °C at 10 °C min^{-1}. The temperature and sensitivity of the DSC was calibrated using In, Zn, Sn, Bi and CsCl reference materials, resulting in a temperature accuracy of ± 0.2 °C, while the balance has an accuracy of ± 20 µg.

Temperature Programmed Photographic Analysis (TPPA)

A pellet of $LiB_{11}H_{14}{\cdot}2H_2O$ and α-$LiB_{11}H_{14}{\cdot}(H_2O)_n$ (50 mg, 6 mm diameter) were pressed at 700 MPa inside an argon glovebox, transferred to a glass tube under an argon atmosphere and placed in a custom-made brass heating block. The sample was heated from RT to ≈ 230 °C ($\Delta T/\Delta t$ = 10 °C min^{-1}) while photos of the sample were collected every five seconds.

Electrochemical Impedance Spectroscopy (EIS)

Pellets of each sample (50 mg) were pressed at 700 MPa (6 mm in diameter, ≈ 1.4 mm in thickness) inside an argon glovebox, sandwiched between gold foil (0.1 mm in thickness), and sealed within an airtight 'Swagelok-type' Teflon cell with 316 stainless steel electrodes. The measurements were performed using a ZIVE SP1 electrochemical workstation at 100 mV AC from 10 Hz to 1 MHz at RT and at isothermal temperatures after heating and cooling by maintaining 50 minutes of thermal equilibrium at each temperature. Temperature was monitored by a K-type thermocouple ≈ 5 mm from the pellet and controlled with a tube furnace from 30 – 90 °C and 90 – 30 °C for samples $LiB_{11}H_{14}{\cdot}2H_2O$ and α-$LiB_{11}H_{14}{\cdot}(H_2O)_n$ with 10 °C steps. This measurement was performed four times for sample α-$LiB_{11}H_{14}{\cdot}(H_2O)_n$, and after each cycle the Swagelok cell was opened inside an argon glovebox, and the pellet

thickness was measured. Each cycle was performed after an interval of 24 hours at RT. Sample $LiB_{11}H_{14}$ was heated from 30 – 110 °C in intervals of 10 °C. Ionic conductivity data (σ) was derived from the equation: $\sigma = d/IA$, where σ is the ionic conductivity in S cm^{-1}, d is the pellet thickness in cm, I is the x-intercept of the Nyquist blocking tail, and A is the area of the pellet face in cm^2. This tail accounts for the diffusion of ions in the solid-state electrolyte.[5] The measurement uncertainty on each ionic conductivity data point (± 10 %) is based on the x-intercept of the Nyquist plot and has little impact on the logarithmic-scale of ionic conductivity, which spans many orders of magnitude.[6] The activation energy of α-$LiB_{11}H_{14}\cdot(H_2O)_n$ was determined from the slope of the solid-state ionic conductivity plot between 55 and 85 °C (Fig. 3B) for cycles 1 and 4 and averaged using the Arrhenius equation: $\ln \sigma_{ion} = \ln \sigma_o - (E_a/K_BT)$, where σ_o is a pre-exponential factor (S cm^{-1}), E_a the activation energy (J), K_B the Boltzmann constant (1.3806 x 10^{-23} J K^{-1}), and T the temperature (K).[2,6]

Linear Sweep Voltammetry (LSV)

This experiment was performed to determine the oxidative stability limit of α-$LiB_{11}H_{14}\cdot(H_2O)_n$ against Li metal, and it was based on a method proposed by Han *et. al.*[7] and Asakura *et. al.*[8] α-$LiB_{11}H_{14}\cdot(H_2O)_n$ was mixed with graphite, previously heated to 550 °C under vacuum for 12 h, in a weight ratio of 75:25 by grinding 5 times with a mortar and pestle. 3 mg of the mixture was layered on top of 40 mg of the sample, which was pressed together at 700 MPa under argon to form a two layered pellet. This pellet was sandwiched to form an Al/Pt/sample+C/sample/Li configuration, which was sealed within an airtight 'Swagelok-type' Teflon cell. LSV was conducted at 30 °C with a scan rate of 50 µV s^{-1} from 1.4 V to 6.4 V. A second LSV cycle was also conducted from 1.5 to 5.1 V at the same scan rate and temperature. The oxidative stability of the material was determined from the intersection point of two linear lines with $R^2 > 0.99$ (the background and the oxidative current).[8]

Galvanostatic Cycling (GC)

All galvanostatic measurements were performed on a Landt Instruments Battery Testing System using a coin cell or a Swagelok-type cell at 60 °C. All cells were prepared by pressing a pellet of the solid-state electrolyte (SSE), α-$LiB_{11}H_{14}\cdot(H_2O)_n$ (30 mg) at 700 MPa (6 mm in diameter, ≈ 1.0 mm in thickness, 0.28 cm^2 in surface area) inside an argon glovebox. The coin cell of Li/α-$LiB_{11}H_{14}\cdot(H_2O)_n$/Li was assembled by sandwiching the SSE between pure lithium

disks and placing it inside a coin cell containing a nickel foil and a separator, which was sealed using a coin press machine. Another symmetric cell of *α*-$LiB_{11}H_{14}\cdot(H_2O)_n$ was prepared in a Swagelok-type assembly with the addition of 1 drop of liquid electrolyte lithium hexafluorophosphate solution in ethylene carbonate and dimethyl carbonate (1.0 M $LiPF_6$ EC/DMC (*v/v* = 50/50)) on top of each side of the SSE and sandwiched between lithium disks to form a Li/LE/*α*-$LiB_{11}H_{14}\cdot(H_2O)_n$/LE/Li cell. Another cell was prepared with the addition of 1 mg of ionic liquid (IL) $LiB_{11}H_{14}\cdot 2H_2O$ on each side of the SSE *α*-$LiB_{11}H_{14}\cdot(H_2O)_n$ (28 mg), which was pressed together at 700 MPa (6 mm in diameter, ≈ 1.0 mm in thickness, 0.28 cm^2 in surface area). This pellet was sandwiched between lithium disks to form a Li/IL/*α*-$LiB_{11}H_{14}\cdot(H_2O)_n$/IL/Li cell. All batteries were left for 12 h at 60 °C at open circuit voltage prior to the commencement of the measurements. A constant current density of 25 μA cm^{-2} was applied for 1 hour in each direction during 48 hours. Then, the current was increased to 50 μA cm^{-2} and left running for 96 hours with 1 hour sweeps. These current densities were chosen to compare with recent literature on other boron-hydrogen systems.[9–11]

Critical Current Density (CCD) Test

The symmetric Li/*α*-$LiB_{11}H_{14}\cdot(H_2O)_n$/Li cell was left for 12 h at 60 °C at open circuit voltage. A constant current of 25 μA cm^{-2} was applied for 30 minutes at each direction during 5 hours. Then the current was raised up to 750 μA cm^{-2} with increases of 25 μA cm^{-2} steps and left at each current density for 5 hours with 30 minutes sweeps, following a similar methodology proposed by Su *et. al.*[12]

Battery Assembly and Electrochemical Measurements

All measurements were performed on a Landt Instruments Battery Testing System using a Swagelok-type cell at 60 °C. The solid-state cell was prepared based on a similar methodology described by Gulino *et. al*.[11] The cathode was prepared by mixing *α*-$LiB_{11}H_{14}\cdot(H_2O)_n$ and TiS_2 in a 1:1 proportion by mass. The mixture was ground 5 times with a mortar and pestle, and 2 mg of the mixture was layered on top of a pellet (6 mm diameter) of 25 mg of *α*-$LiB_{11}H_{14}\cdot(H_2O)_n$, previously pressed at 350 MPa. The cathode loading was chosen to be similar to other recent publications on similar materials.[9,11,13] Both, cathode and solid-electrolyte, were pressed together at 700 MPa. A drop of liquid electrolyte 1.0 M $LiPF_6$ EC/DMC (*v/v* = 50/50) was added on top of a Li metal disk (6 mm diameter) that was used as the anode and

hand-pressed together with the pellet of SSE and cathode in a Swagelok-type cell against the stainless steel electrodes, resulting in the Li/LE/*α*-$LiB_{11}H_{14}\cdot(H_2O)_n$/*α*-$LiB_{11}H_{14}\cdot(H_2O)_n$+$TiS_2$ assembly. The cell containing ionic liquid at the interface was prepared by pressing a pellet (6 mm diameter) of 1 mg of $LiB_{11}H_{14}\cdot 2H_2O$ on each side of the SSE *α*-$LiB_{11}H_{14}\cdot(H_2O)_n$ (23 mg) at 350 MPa. Both, cathode (2 mg) and electrolyte, were pressed together at 700 MPa and hand-pressed with lithium resulting in a Li/IL/*α*-$LiB_{11}H_{14}\cdot(H_2O)_n$/IL/*α*-$LiB_{11}H_{14}\cdot(H_2O)_n$+$TiS_2$ cell. Galvanostatic charge/discharge experiments (1 *C* = 239 mA g^{-1}) were conducted with the cell at 60 °C in the voltage range 1.7 – 2.5 V vs Li^+/Li. Only the mass of TiS_2 was considered for the calculation of the specific capacity.

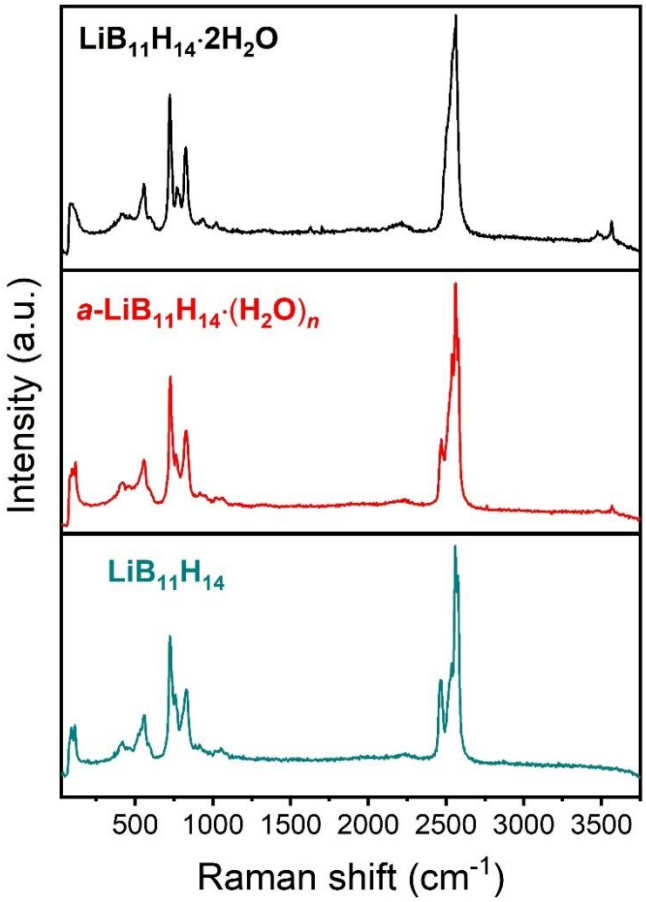

Figure S1. Raman spectra of solid-state $LiB_{11}H_{14}\cdot 2H_2O$ (black), *α*-$LiB_{11}H_{14}\cdot(H_2O)_n$ (red), and $LiB_{11}H_{14}$ (green).

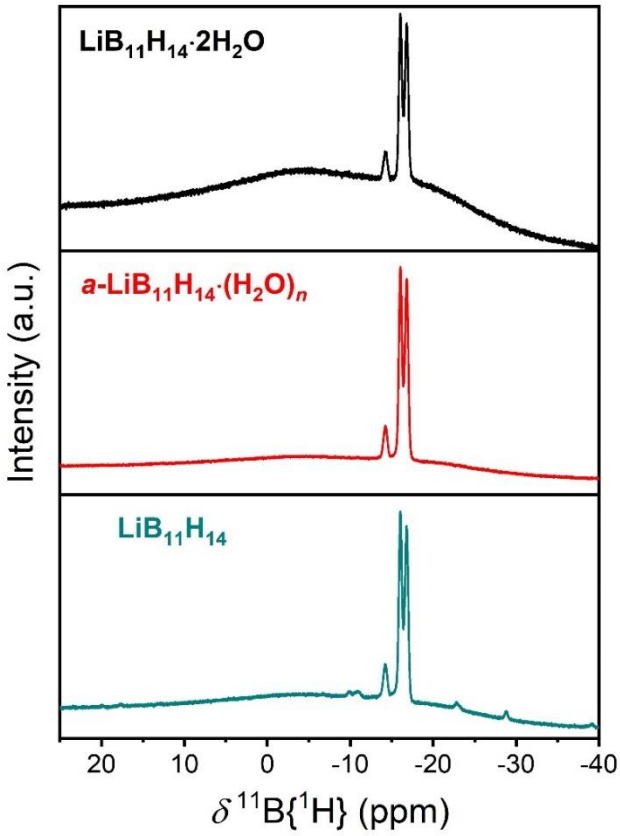

Figure S2. $^{11}B\{^1H\}$ NMR spectra (128 MHz) of $LiB_{11}H_{14}\cdot 2H_2O$ (black), *α*-$LiB_{11}H_{14}\cdot(H_2O)_n$ (red), and $LiB_{11}H_{14}$ (green) in CD_3CN. The resonances at δ = −14.2, −16.0 and −16.8 ppm that are observed in all spectra are due to $B_{11}H_{14}^-$. $B_{11}H_{13}OH^-$ (δ = 18.8, −9.6, −10.7, −23.3, −29.1, and −40.0 ppm) can be identified in the spectra of $LiB_{11}H_{14}$ by small intensity peaks.

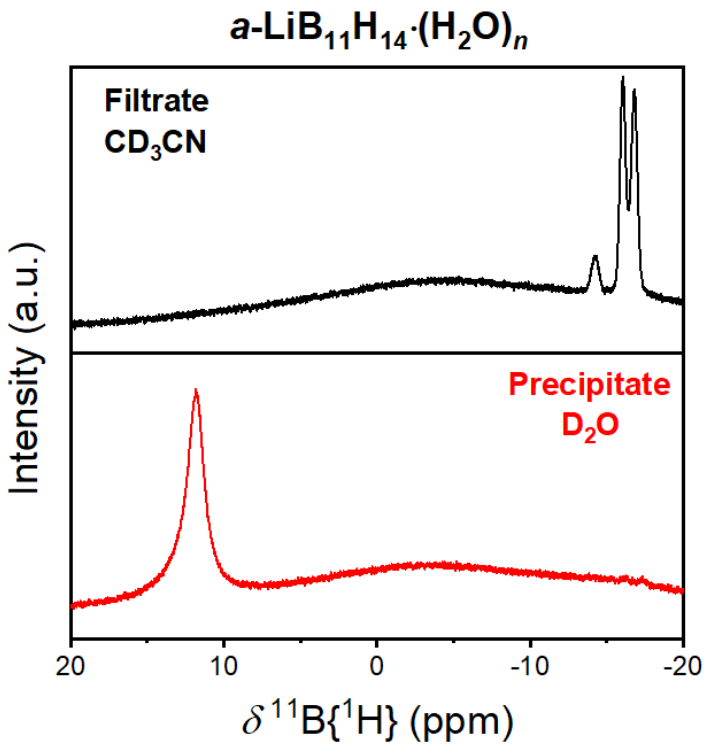

Figure S3. $^{11}B\{^1H\}$ NMR spectra (128 MHz) of filtrate in CD_3CN (top) and precipitate in D_2O (bottom) after mixing *a*-$LiB_{11}H_{14}\cdot(H_2O)_n$ in acetonitrile. The $^{11}B\{^1H\}$ NMR spectrum of the filtrate shows the presence of $B_{11}H_{14}^-$ anion (δ = −14.2, −16.0 and −16.8 ppm), whereas the precipitate shows the presence of a borate species at 11.8 ppm.

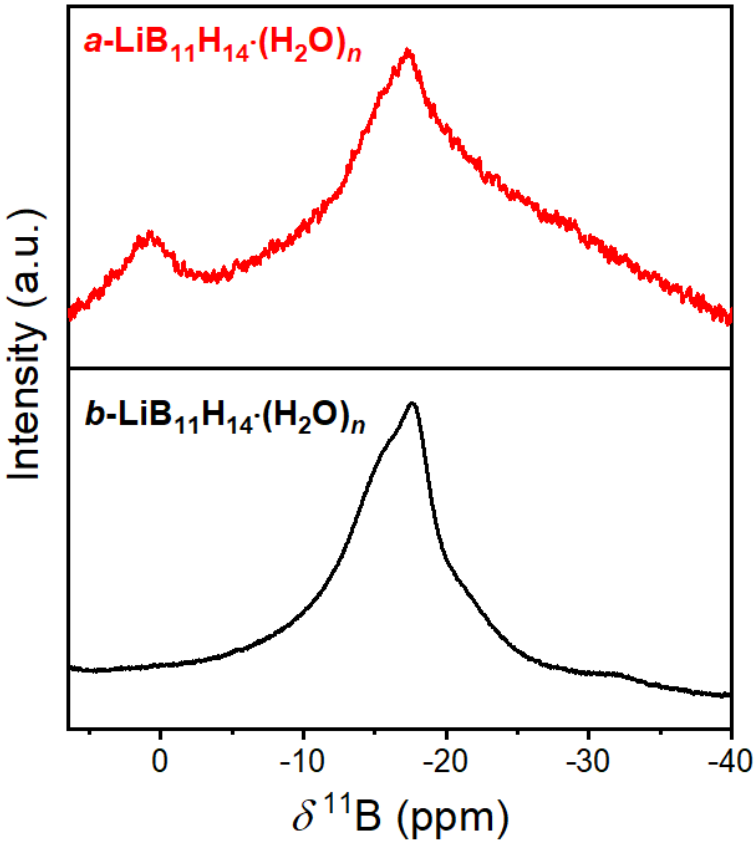

Figure S4. Solid-state ^{11}B MAS NMR spectra of *a*-$LiB_{11}H_{14}\cdot(H_2O)_n$ (red) and *b*-$LiB_{11}H_{14}\cdot(H_2O)_n$ (black), which was added for comparison to show the position of $B_{11}H_{14}^-$ (δ = -15.4 and -17.7 ppm), at RT.[6,10] The presence of a borate species can be seen in the spectrum of *a*-$LiB_{11}H_{14}\cdot(H_2O)_n$ at ≈ 1 ppm.

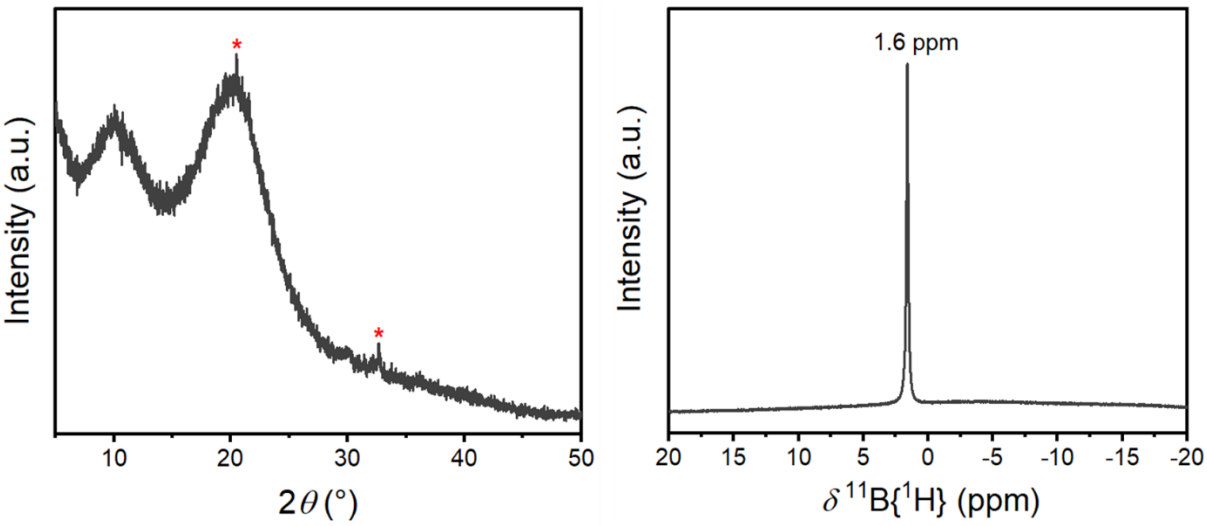

Figure S5. XRPD (λ = 1.54056 Å) pattern (left) and $^{11}B\{^1H\}$ NMR spectrum (128 MHz) in D_2O (right) for the product of the reaction of LiOH and H_3BO_3 at RT. Red stars in the XRPD pattern at 2Θ = 20.5° and 32.6° represent unreacted LiOH and the broad diffraction halos at ≈ 10° and ≈ 20° 2Θ are due to the sample holder, but may mask other amorphous halos.

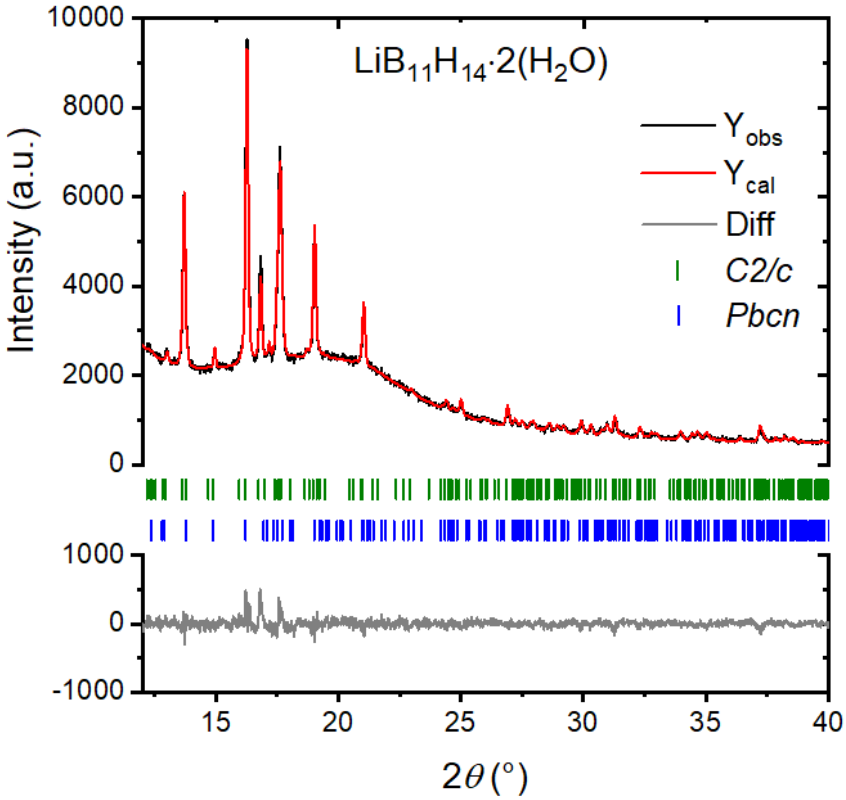

Figure S6. XRPD (λ = 1.54056 Å) and Rietveld refinement of $LiB_{11}H_{14}{\cdot}2H_2O$. R_{wp} = 3.71 %. Green and blue lines represent Bragg position from space group *C*2/*c* ($LiB_{11}H_{14}{\cdot}2H_2O$),[6] 97.0(3) wt%, and the indexed space group *Pbcn* ($LiB_{11}H_{14}{\cdot}(H_2O)_n$), 3.0(3) wt%, respectively.

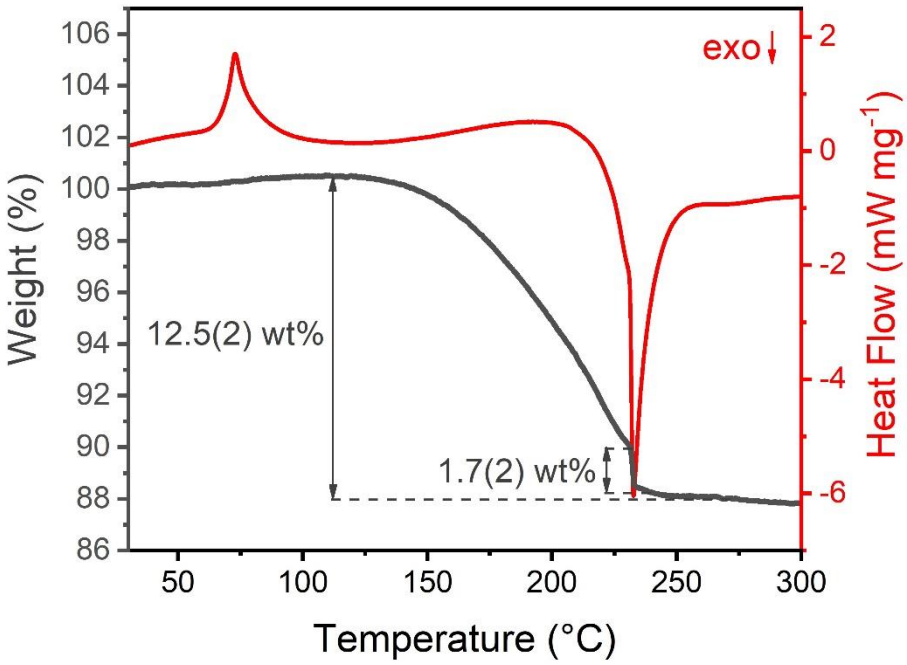

Figure S7. DSC/TGA measurement of $LiB_{11}H_{14}{\cdot}2H_2O$ in the temperature range 30 – 300 °C ($\Delta T/\Delta t$ = 10 °C min^{-1}, Ar flow = 40 mL min^{-1}). Approximately 7 mg of sample was used for analysis. The melting event is characterised by the endothermic feature at 73 °C, and the exothermic peak at 233 °C represents its decomposition accompanied by a mass loss of 12.5(2)%.

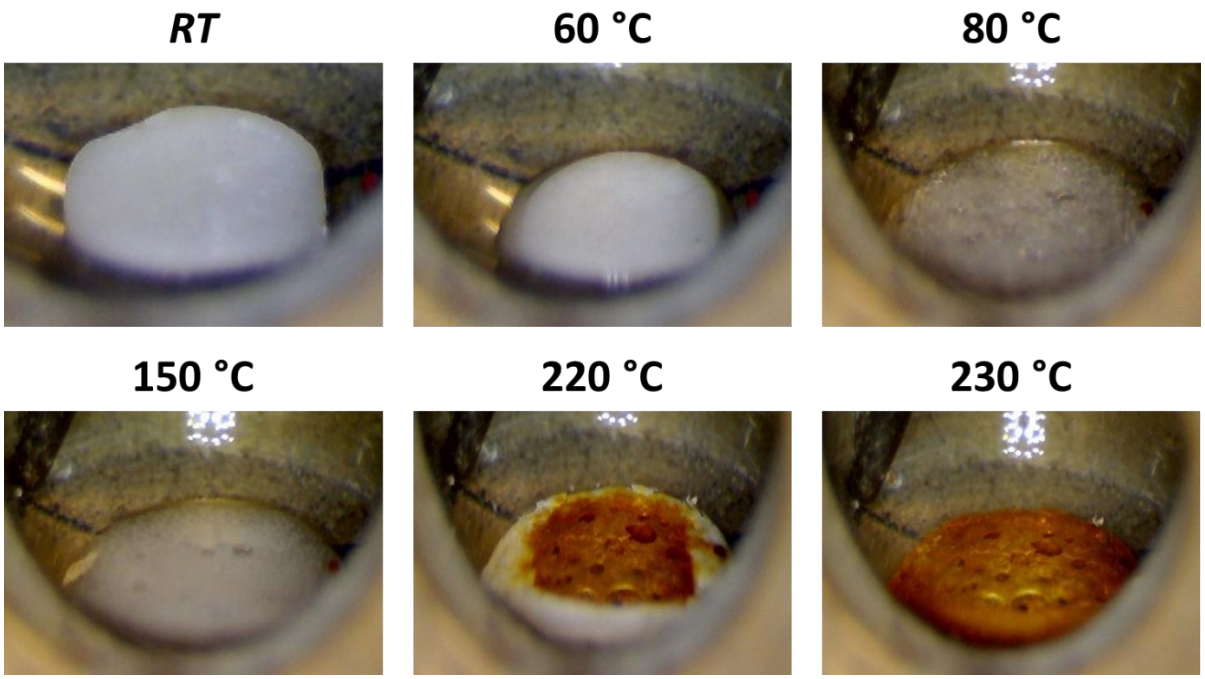

Figure S8. TPPA of $LiB_{11}H_{14}{\cdot}2H_2O$ heated from RT to 230 °C ($\Delta T/\Delta t$ = 10 °C min^{-1}). The sample starts melting at ≈ 60 °C, solidifies again upon heating, and starts decomposing at ≈ 220 °C, when it becomes a yellow solid.

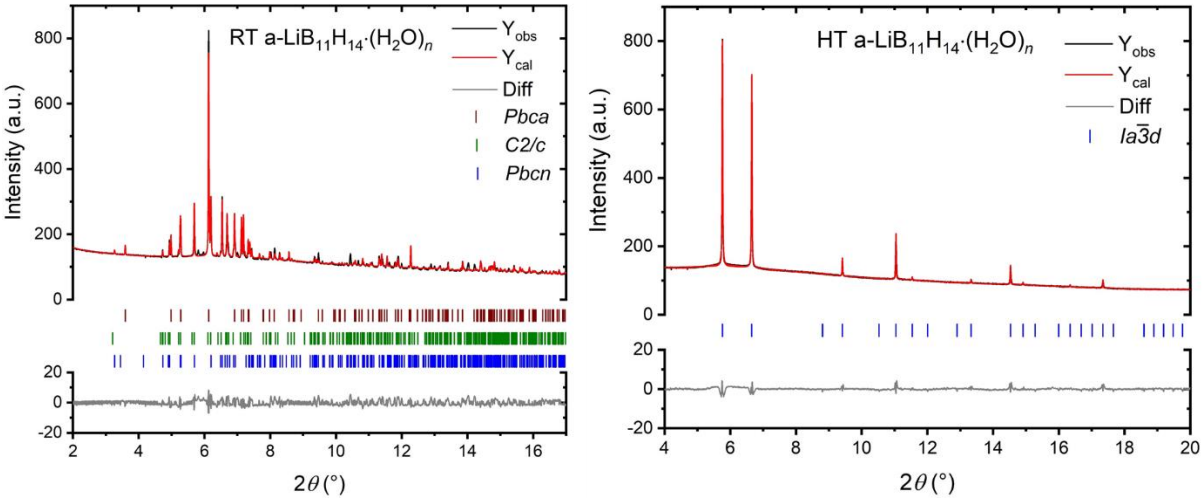

Figure S9. Left: SR-XRPD (λ = 0.590827(4) Å) and Rietveld refinement of sample α-$LiB_{11}H_{14}\cdot(H_2O)_n$ at RT, R_{wp} = 5.37%. Brown, green and blue lines indicate Bragg positions from space groups *Pbca* ($LiB_{11}H_{14}$),[9] 70.0(1) wt%, *C2/c* ($LiB_{11}H_{14}\cdot 2H_2O$),[6] 4.10(11) wt%, and the indexed space group *Pbcn* ($LiB_{11}H_{14}\cdot(H_2O)_n$), 25.9(1) wt%, respectively. Right: SR-XRPD (λ = 0.590827(4) Å) and Rietveld refinement of α-$LiB_{11}H_{14}\cdot(H_2O)_n$ at 100 °C, R_{wp} = 3.08%. Blue lines indicate Bragg position from space group $Ia\bar{3}d$.

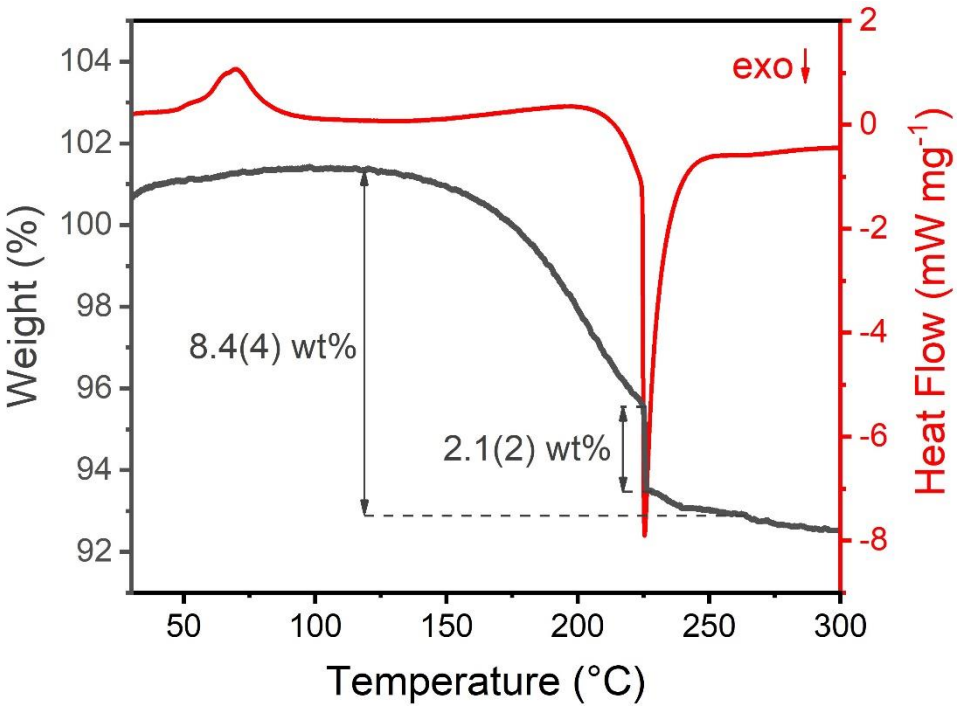

Figure S10. DSC/TGA measurement of α-$LiB_{11}H_{14}\cdot(H_2O)_n$ in the temperature range 30 – 300 °C ($\Delta T/\Delta t$ = 10 °C min^{-1}, Ar flow = 40 mL min^{-1}). Approximately 7 mg of sample was used for analysis. The phase change event is characterised by the endothermic feature at 70 °C, and the exothermic peak at 225 °C represents its decomposition accompanied by a mass loss of 8.4(4)%.

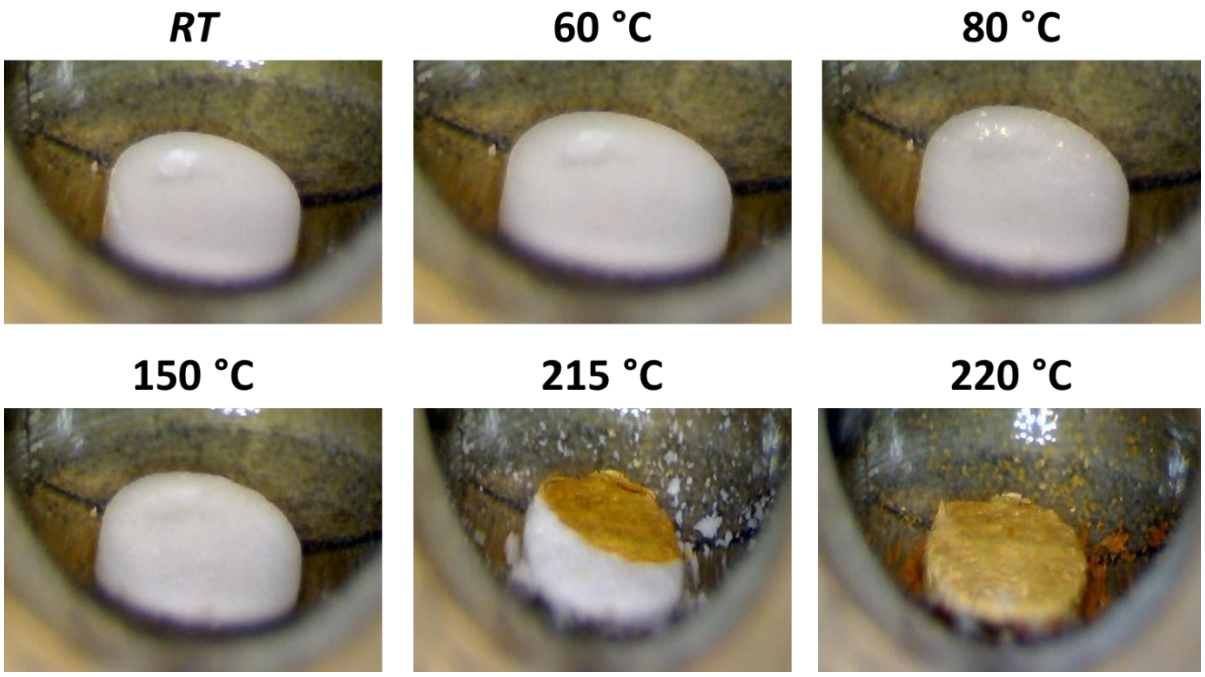

Figure S11. TPPA of α-$LiB_{11}H_{14}\cdot(H_2O)_n$ heated from RT to 220 °C ($\Delta T/\Delta t$ = 10 °C min^{-1}). The sample changes phase near 70 °C, and it does not melt. The pellet expands and keeps its solid shape upon heating. It starts decomposing at ≈ 215 °C, when it becomes a yellow solid.

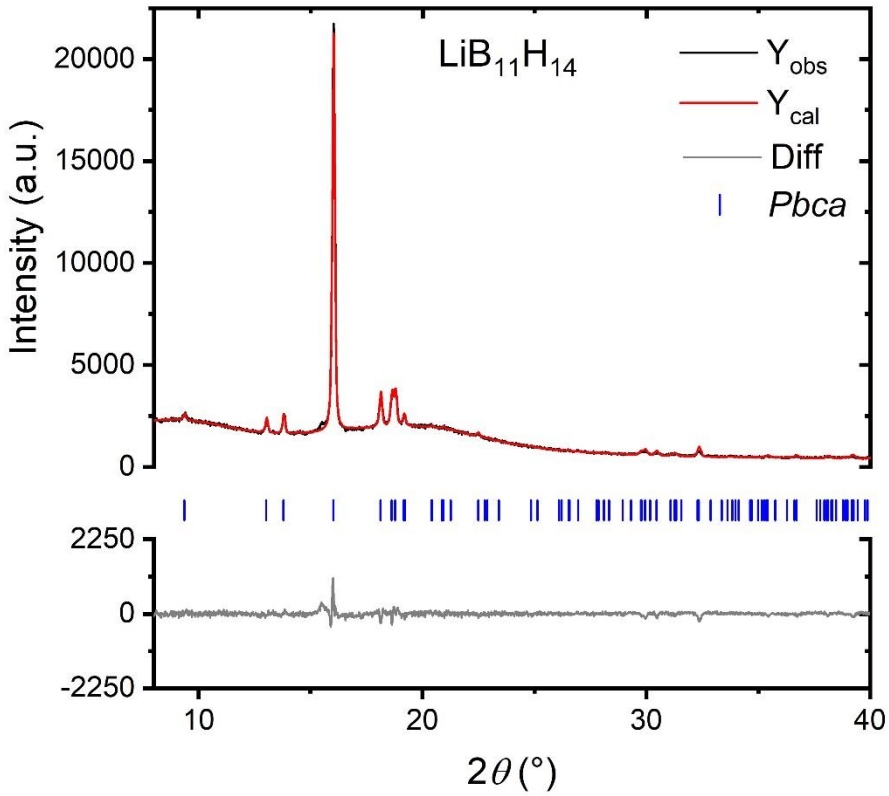

Figure S12. XRPD (λ = 1.54056 Å) and Rietveld refinement of $LiB_{11}H_{14}$. R_{wp} = 4.05%. Blue lines represent Bragg position from space group *Pbca*.[9]

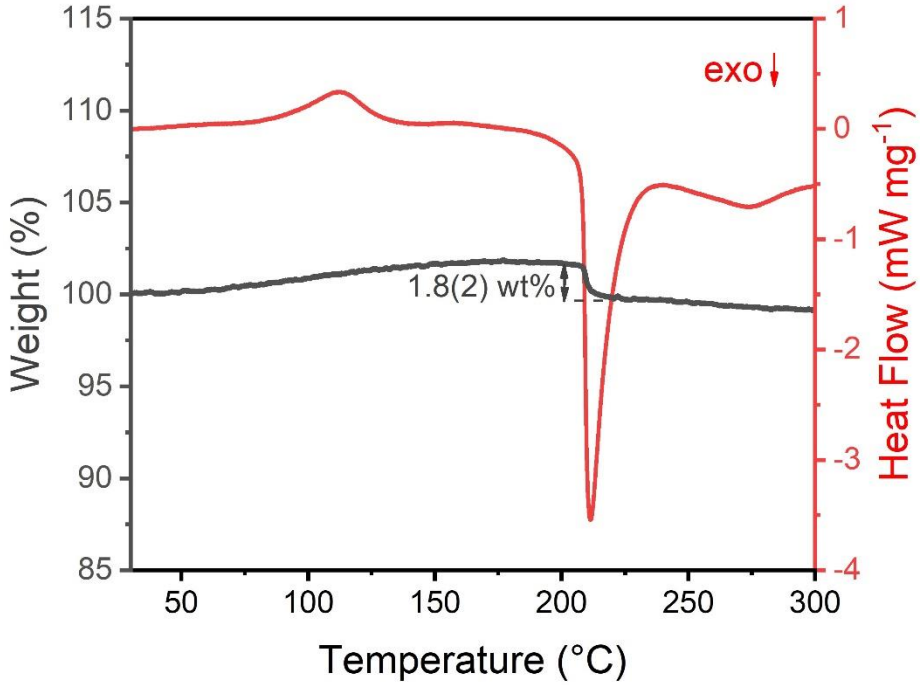

Figure S13. DSC/TGA measurement of $LiB_{11}H_{14}$ in the temperature range 30 – 300 °C ($\Delta T/\Delta t$ = 10 °C min^{-1}, Ar flow = 40 mL min^{-1}). Approximately 7 mg of sample was used for analysis. The phase change event is characterised by the endothermic feature at 112 °C, and the exothermic peak at 211 °C represents its decomposition accompanied by a mass loss of 1.8(2)%.

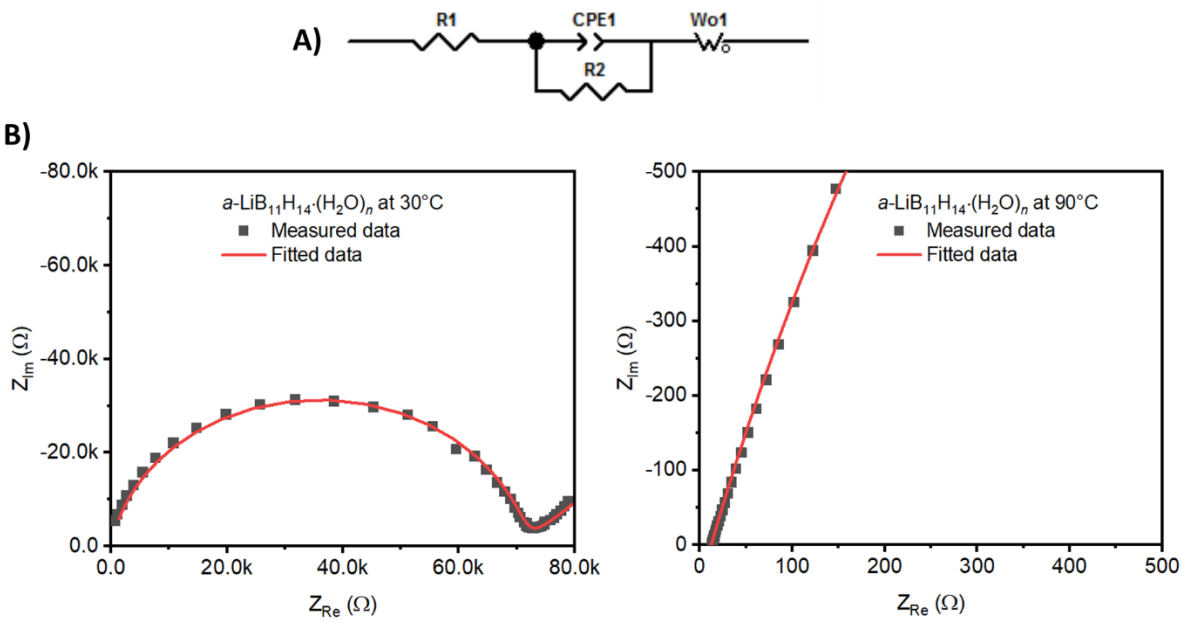

Figure S14. A) Equivalent circuit model used to fit impedance data (R1+Q1/R2+Wo), where R1 is the internal resistance, R2 is the surface-layer resistance, CPE1 (Q1) is the constant phase element and Wo1 is the open Warburg element.[14,15] B) Nyquist plots of the Au-symmetric cell for *a*-$LiB_{11}H_{14}\cdot(H_2O)_n$ at 30 and 90 °C.

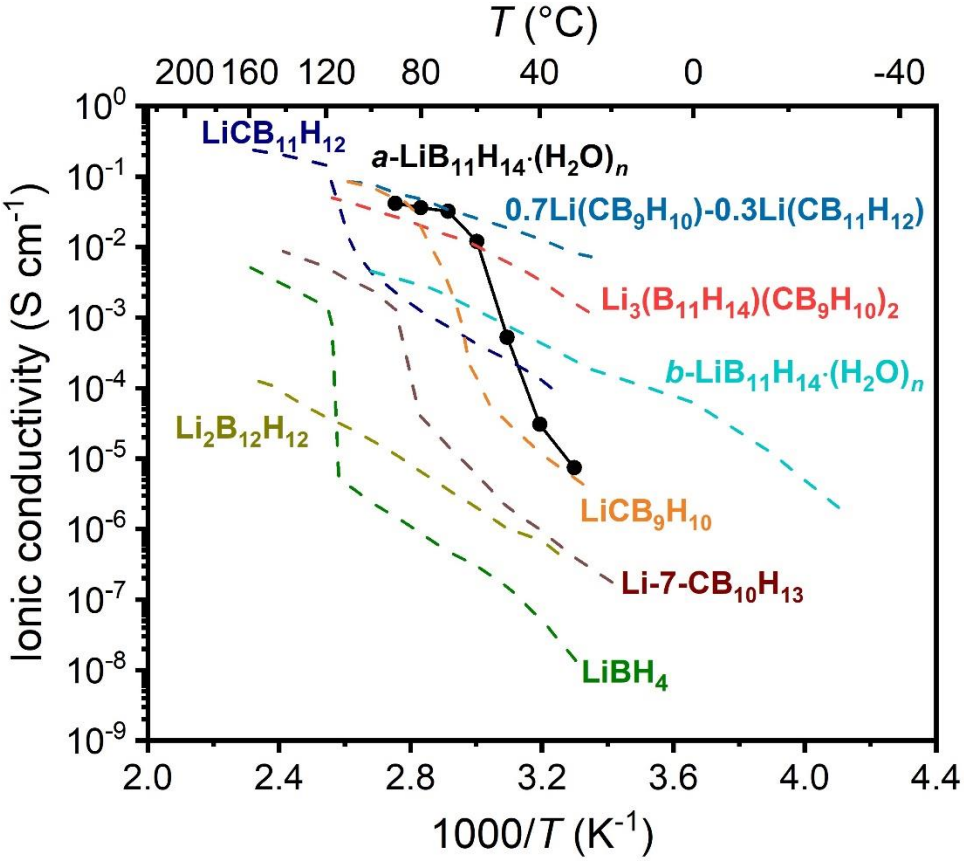

Figure S15. Solid-state ionic conductivity of *a*-$LiB_{11}H_{14}\cdot(H_2O)_n$ compared with other lithium boron-hydrogen salts.[6,9,13,16–20]

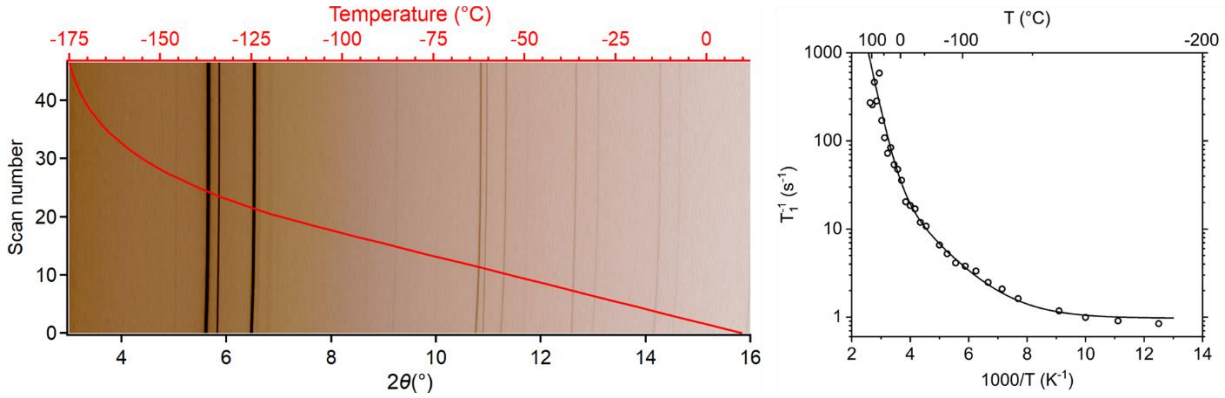

Fig. S16. Left: *In-situ* SR-XRPD (λ = 0.563516(6) Å) data of *b*-$LiB_{11}H_{14}\cdot(H_2O)_n$ during cooling at 1 °C min^{-1}. No significant change can be observed in the temperature range used to conduct the experiment (RT to -175 °C). Red line represents temperature. Right: ^{11}B spin-lattice relaxation rates of *b*-$LiB_{11}H_{14}\cdot(H_2O)_n$ as a function of inverse temperature. The solid line represents the best model fit to a relaxation model considering two types of dynamic processes with different activation energies and a temperature-independent contribution to relaxation due to interactions with paramagnetic impurities in the sample.

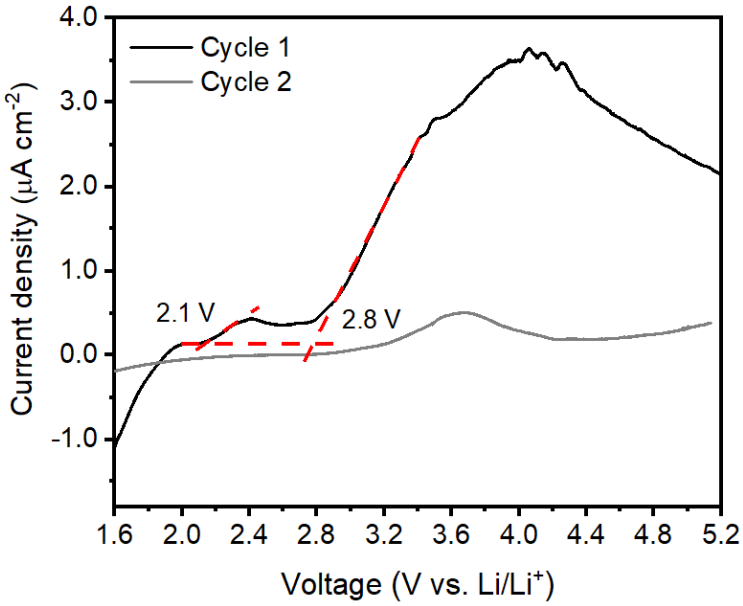

Figure S17. Linear Sweep Voltammogram of Li/*α*-$LiB_{11}H_{14}\cdot(H_2O)_n$/*α*-$LiB_{11}H_{14}\cdot(H_2O)_n$+C/Pt/Al cells at a scan rate of 50 μV s^{-1} at 30 °C between 1.6 and 5.2 V (1st cycle) and 1.6 and 5.1 V (2nd cycle). The oxidative limit was estimated by the interception of the red dashed lines, which represent the linear regression lines of the background and the anodic current.

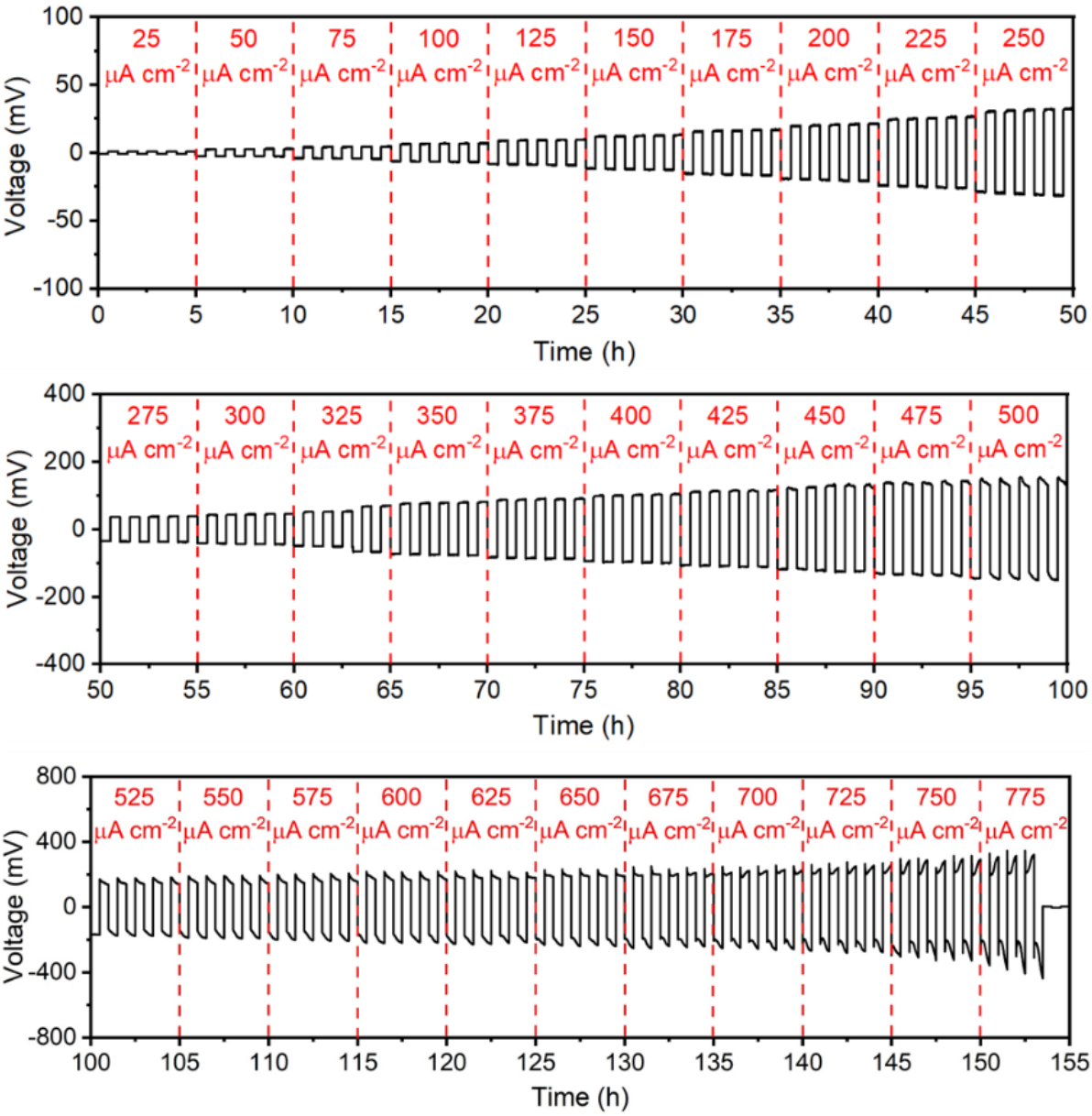

Figure S18. Endurable time control measurement used to identify the critical current density of the Li/a-$LiB_{11}H_{14}\cdot(H_2O)_n$/Li symmetric cell at 60 °C from 25 to 775 μA cm^{-2}. Short circuit failure happens at 775 μA cm^{-2}, therefore the CCD is determined to be 750 μA cm^{-2}.

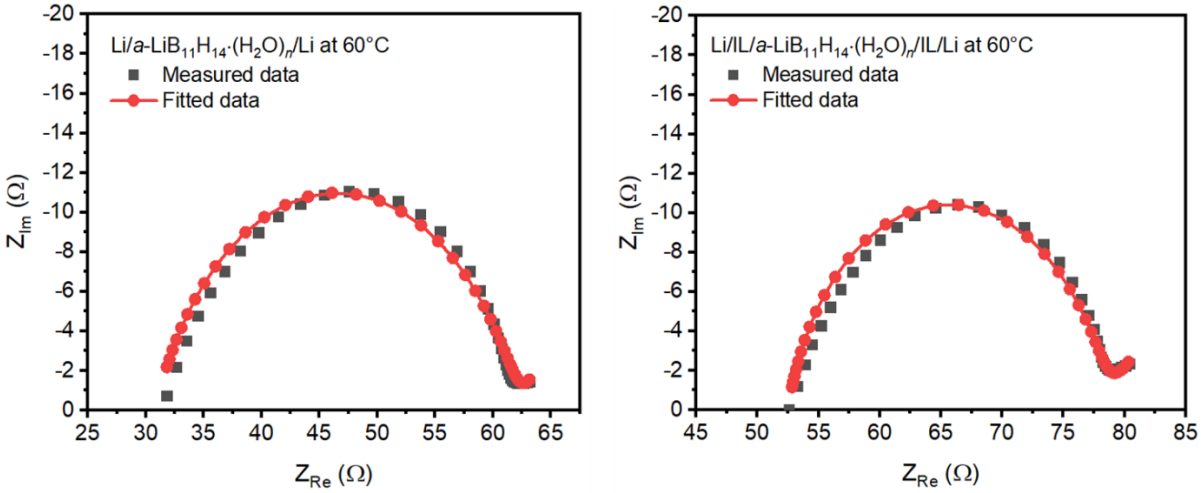

Figure S19. Nyquist plots of the Li-symmetric cell (Swagelok-type) for *a*-$LiB_{11}H_{14}\cdot(H_2O)_n$ after 1 hour stabilisation at 60 °C with (right) and without (left) addition of the ionic liquid ($LiB_{11}H_{14}\cdot 2H_2O$) at the interface Li/SSE. Data was fitted using the equivalent circuit model (*R*1+*Q*1/*R*2+*W*o) presented in Fig. S14A.

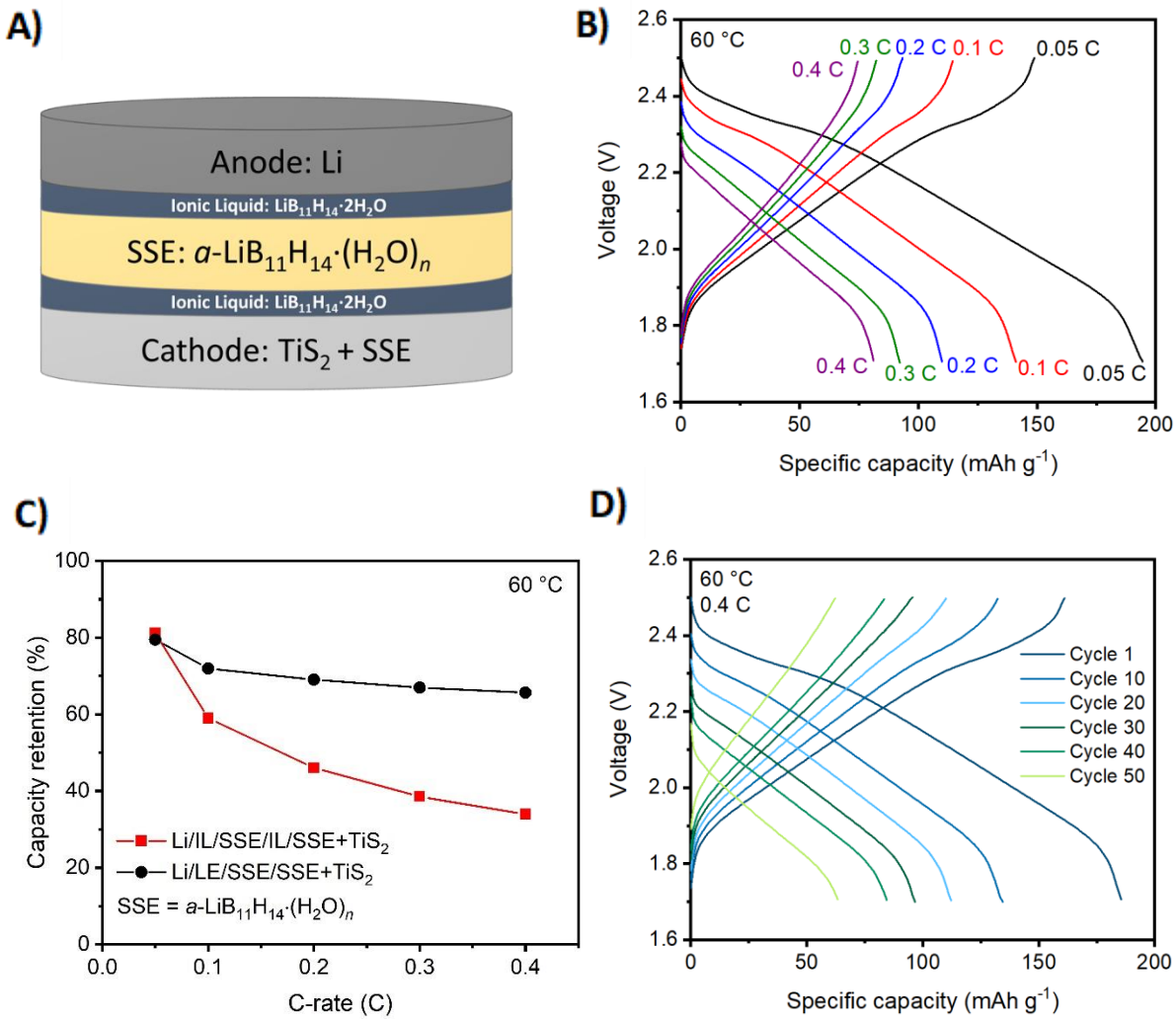

Fig. S20. A) Schematic representation of the solid-state battery Li/IL/*a*-$LiB_{11}H_{14}\cdot(H_2O)_n$/IL/*a*-$LiB_{11}H_{14}\cdot(H_2O)_n$+$TiS_2$ in a Swagelok-type cell. B) Discharge/charge profiles at 0.05, 0.1, 0.2, 0.3 and 0.4 *C* (1.7 – 2.5 V) at 60 °C. C) Capacity retention at different *C*-rates compared to the cell of Li/LE/*a*-$LiB_{11}H_{14}\cdot(H_2O)_n$/*a*-$LiB_{11}H_{14}\cdot(H_2O)_n$+$TiS_2$. D) Discharge/charge profiles at 0.4 *C* for 50 cycles at 60 °C.

Table S1: Structural parameters determined from Rietveld refinement of the XRPD data from this work and other related compounds.

Sample	*T* (°C)	Space Group and Lattice Parameters
$LiB_{11}H_{14}\cdot 2H_2O$	25	*C2/c* ($LiB_{11}H_{14}\cdot 2H_2O$),[6] 97.0(3) wt% Monoclinic *a* = 10.431(3) Å *b* = 10.110(3) Å *c* = 42.329(10) Å *β* = 91.212(3)° *V* = 4463.1(19) Å^3 Z = 16 *Pbcn* ($LiB_{11}H_{14}\cdot(H_2O)_n$), 3.0(3) wt% Orthorhombic *a* = 41.431(30) Å *b* = 10.114(8) Å *c* = 10.454(11) Å *V* = 4380.8(64) Å^3 Z = 16
α-$LiB_{11}H_{14}\cdot(H_2O)_n$	25	*Pbca* ($LiB_{11}H_{14}$),[9] 70.0(1) wt% Orthorhombic *a* = 9.7999(1) Å *b* = 9.5073(1) Å *c* = 18.856(1) Å *V* = 1756.8(1) Å^3 Z = 8 *Pbcn* ($LiB_{11}H_{14}\cdot(H_2O)_n$), 25.9(1) wt% Orthorhombic *a* = 41.446(1) Å *b* = 10.127(1) Å *c* = 10.440(1) Å *V* = 4382.0(2) Å^3 Z = 16 *C2/c* ($LiB_{11}H_{14}\cdot 2H_2O$),[6] 4.10(11) wt% Monoclinic *a* = 10.421(1) Å *b* = 10.142(1) Å *c* = 42.295(3) Å *β* = 91.097(6)° *V* = 4469.1(7) Å^3 Z = 16
α-$LiB_{11}H_{14}\cdot(H_2O)_n$	100	$Ia\bar{3}d$ Cubic *a* = 14.399(1) Å *V* = 2985.6(1) Å^3 Z = 12

$LiB_{11}H_{14}$	25	*Pbca* ($LiB_{11}H_{14}$)[9] Orthorhombic *a* = 9.786(2) Å *b* = 9.5241(19) Å *c* = 18.892(4) Å *V* = 1760.8(6) Å^3 Z = 8

Table S2: Pellet thickness at RT and ionic conductivity results at 30 and 90 °C for sample *α*-$LiB_{11}H_{14}\cdot(H_2O)_n$ at different cycles.

Cycle	Pellet thickness at RT before cycle (mm)	Ionic conductivity at 30 °C (S cm^{-1})	Ionic conductivity at 90 °C (S cm^{-1})	Pellet thickness at RT after cycle (mm)
1	1.4 (± 0.1)	7.4 x 10^{-6}	4.2 x 10^{-2}	1.2 (± 0.1)
2	1.2 (± 0.1)	6.0 x 10^{-6}	2.3 x 10^{-2}	1.2 (± 0.1)
3	1.2 (± 0.1)	8.6 x 10^{-6}	2.4 x 10^{-2}	1.2 (± 0.1)
4	1.2 (± 0.1)	7.7 x 10^{-6}	3.6 x 10^{-2}	1.1 (± 0.1)

Table S3: Activation energy of some lithium boron-hydrogen salts.

Lithium boron-hydrogen salt	Activation energy (eV)	Reference
HT[a] *α*-$LiB_{11}H_{14}\cdot(H_2O)_n$	0.16 (± 0.01)	This work
$LiCB_9H_{10}$	0.29	[16]
$LiCB_{11}H_{12}$	0.22	[17]
$0.7Li(CB_9H_{10})$-$0.3Li(CB_{11}H_{12})$	0.29	[13]
Li-7-$CB_{10}H_{13}$	0.39	[18]
***b*-$LiB_{11}H_{14}\cdot(H_2O)_n$**	0.5	[6]
$Li_2B_{11}H_{12}$	0.49	[21]
LT[b] $LiB_{11}H_{14}$	0.81	[9]
HT $LiB_{11}H_{14}$	0.16	[9]
LT $LiBH_4$	0.69	[19]
HT $LiBH_4$	0.53	[19]

[a]HT = High Temperature polymorph. [b]LT = Low Temperature polymorph

Table S4: Interfacial resistance for the systems Li/IL/*α*-$LiB_{11}H_{14}\cdot(H_2O)_n$/IL/Li (IL = $LiB_{11}H_{14}\cdot 2H_2O$) and Li/*α*-$LiB_{11}H_{14}\cdot(H_2O)_n$/Li and circuit component values *R*1 and *R*2 from Nyquist plots shown in Fig. S19.

	R1 (Ω)	R2 (Ω)	R_{SEI} (Ω cm^2)
Li/SSE/Li	30.8 ± 0.7	31.1 ± 2.1	4.4 ± 0.3
Li/IL/SSE/IL/Li	52.5 ± 0.5	25.7 ± 1.5	3.6 ± 0.2

REFERENCES

1 A. V. Skripov, R. V. Skoryunov, A. V. Soloninin, O. A. Babanova, V. Stavila and T. J. Udovic, *J. Phys. Chem. C*, 2018, **122**, 3256–3262.

2 A. Gradišek, M. Krnel, M. Paskevicius, B. R. S. Hansen, T. R. Jensen and J. Dolinšek, *J. Phys. Chem. C*, 2018, **122**, 17073–17079.

3 A. Gradišek, M. Jørgensen, M. Paskevicius, B. R. S. Hansen and T. R. Jensen, *J. Phys. Chem. C*, 2021, **125**, 5534–5541.

4 I. C. Madsen, N. V. Y. Scarlett, R. Kleeberg and K. Knorr, *Int. Tables Crystallogr.*, 2019, **H**, 344–373.

5 B. R. S. Hansen, M. Paskevicius, M. Jørgensen and T. R. Jensen, *Chem. Mater.*, 2017, **29**, 3423–3430.

6 D. H. P. Souza, K. T. Møller, S. A. Moggach, T. D. Humphries, A. M. D'Angelo, C. E. Buckley and M. Paskevicius, *J. Mater. Chem. A*, 2021, **9**, 15027–15037.

7 F. Han, Y. Zhu, X. He, Y. Mo and C. Wang, *Adv. Energy Mater.*, 2016, **6**, 1501590.

8 R. Asakura, L. Duchêne, R. S. Kühnel, A. Remhof, H. Hagemann and C. Battaglia, *ACS Appl. Energy Mater.*, 2019, **2**, 6924–6930.

9 S. H. Payandeh, D. Rentsch, Z. Łodziana, R. Asakura, L. Bigler, R. Černý, C. Battaglia and A. Remhof, *Adv. Funct. Mater.*, 2021, **31**, 2010046.

10 S. Payandeh, R. Asakura, P. Avramidou, D. Rentsch, Ł. Zbigniew, C. Radovan, A. Remhof and C. Battaglia, *Chem. Mater.*, 2020, **32**, 1101–1110.

11 V. Gulino, M. Brighi, F. Murgia, P. Ngene, P. De Jongh, R. Černý and M. Baricco, *ACS Appl. Energy Mater.*, 2021, **4**, 1228–1236.

12 J. Su, X. Huang, Z. Song, T. Xiu, M. E. Badding, J. Jin and Z. Wen, *Ceram. Int.*, 2019, **45**, 14991–14996.

13 S. Kim, H. Oguchi, N. Toyama, T. Sato, S. Takagi, T. Otomo, D. Arunkumar, N. Kuwata, J. Kawamura and S. Orimo, *Nat. Commun.*, 2019, **10**, 1–9.

14 Y. Bai, X. Wang, X. Zhang, H. Shu, X. Yang, B. Hu, Q. Wei, H. Wu and Y. Song, *Electrochim. Acta*, 2013, **109**, 355–364.

15 C. Song, W. Wang, H. Peng, Y. Wang, C. Zhao, H. Zhang, Q. Tang, J. Lv, X. Du and Y. Dou, *Appl. Sci.*, 2018, **8**, 378.

16 W. S. Tang, M. Matsuo, H. Wu, V. Stavila, W. Zhou, A. A. Talin, A. V Soloninin, R. V Skoryunov, O. A. Babanova, A. V Skripov, A. Unemoto, S. I. Orimo and T. J. Udovic,

Adv. Energy Mater., 2016, **6**, 1502237.

17 W. S. Tang, A. Unemoto, W. Zhou, V. Stavila, M. Matsuo, H. Wu, S. Orimo and T. J. Udovic, *Energy Environ. Sci.*, 2015, **8**, 3637–3645.

18 W. S. Tang, M. Dimitrievska, V. Stavila, W. Zhou, H. Wu, A. A. Talin and T. J. Udovic, *Chem. Mater.*, 2017, **29**, 10496–10509.

19 M. Matsuo, Y. Nakamori, S. Orimo, H. Maekawa and H. Takamura, *Appl. Phys. Lett.*, 2007, **91**, 224103.

20 A. Unemoto, K. Yoshida, T. Ikeshoji and S. Orimo, *Mater. Trans.*, 2016, **57**, 1639–1644.

21 S. Kim, N. Toyama, H. Oguchi, T. Sato, S. Takagi, T. Ikeshoji and S. Orimo, *Chem. Mater.*, 2018, **30**, 386–391.